Weathering of Viama?o granodiorite, south Brazil : Part 2-Initial porosity of un-weathered rock controls porosity development in the critical zone

Bonnet, M.

2023-01-01

Bonnet , M , Caner , L , Siitari-Kauppi , M , Mazurier , A , Mexias , A S , Dani , N & Sardini , P 2023 , ' Weathering of Viama?o granodiorite, south Brazil : Part 2-Initial porosity of un-weathered rock controls porosity development in the critical zone ' , Geoderma , vol. 429 , 116247 . https://doi.org/10.1016/j.geoderma.2022.116247

http://hdl.handle.net/10138/356526
https://doi.org/10.1016/j.geoderma.2022.116247

Geoderma 429 (2023) 116247

Contents lists available at ScienceDirect

Geoderma

journal homepage: www.elsevier.com/locate/geoderma

Weathering of Viamão granodiorite, south Brazil: Part 2 – Initial porosity of un-weathered rock controls porosity development in the critical zone

M. Bonnet [a], L. Caner [a], M. Siitari-Kauppi [b], A. Mazurier [a,b,c], A.S. Mexias [c], N. Dani [c], P. Sardini [a]

[a] Institut de Chimie des Milieux et Matériaux de Poitiers (IC2MP), Université de Poitiers, CNRS, (E2-HydrASA), F-86073 Poitiers, France
[b] University of Helsinki, Department of Chemistry, P.O. Box 55, 00014 University of Helsinki, Finland
[c] Instituto de Geociências, Universidade Federal do Rio Grande do Sul – UFRGS, 91501-970 Porto Alegre, RS, Brazil

ARTICLE INFO

Handling Editor: Alberto Agnelli

Keywords:
Weathering
Porosity
Microcracks
Macrocracks
Crack aperture
Autoradiography

ABSTRACT

The development of porosity during rock weathering is a key process controlling nutrients release, water holding capacity available for plants and water flow. Here we used X-ray Computed Tomography (XRCT) and ^{14}C PolyMethylMethAcrylate (PMMA) autoradiography to show how cracks are created and enlarged during initial weathering stages (saprock and saprolite) of granodiorite in southern Brazil (Viamão - RS). The physical evolution is characterized by imaging the pore network, using ^{14}C-PMMA and XRCT methods. Combined with bulk porosity measurements, they highlight the increase in porosity with the degree of weathering (un-weathered rock $\Phi = 1.66$ %, saprolite $\Phi = 11.7$ %). This increase is related to the joint increase of the density of the cracks (un-weathered rock $D = 0.28$ mm^{-1}, saprolite $D = 0.94$ mm^{-1}) and of the average opening of the microcracks (un-weathered rock $w = 2.4$ μm, saprolite $w = 3.9$ μm) and macrocracks (un-weathered rock $w = 176$ μm, saprolite $w = 400$ μm). However, these average crack openings do not account for the variability of the openings that govern the flows, characterized here by specific distribution ranging from the submicrometre to the centimetre scale.

The results highlight that the pore network of the un-weathered rock plays a key role in the initial stages or incipient weathering. The density and aperture and cracks increase following the subcritical cracking concept and new pores are formed by chemo-mechanical processes. The presence/absence of initial fractures in the regolith is certainly a key parameter controlling the weathering of different rock types (mafic vs felsic).

1. Introduction

At the Earth's surface, the transformation of rocks by weathering is well described in terms of mineral transformations. However, these transformations are controlled by the accessibility of fluids and solutes to reactional sites (Meunier et al., 2007, Navarre-Sitchler et al., 2013; 2015). As such, characterizing the evolution of the pore network of rocks during weathering plays a major role in the understanding of surface weathering. These evolutions are complex to understand because they require the coupling between geochemistry, transport, and structural evolution of pore space with time (Putnis, 2002; 2009; Jamtveit, 2009, 2011). This contribution is the companion paper of Bonnet et al. (2022). The present paper aims to characterize the transformation of the pore network of Viamão granodiorite (Rio Grande do Sul, Brazil) during weathering. The porosity of igneous bedrock protolith corresponds to inter- and intra-granular microcracks and microporosity formed during post-magmatic cooling, tectonic and early alteration processes (deuteric or hydrothermal alterations). The incipient weathering of minerals is controlled by the total porosity, i.e., the distribution of the connected porosity in the un-weathered rock at the crystal scale (Hochella and Banfield, 1995; Lee et al., 1995, 1998; Sardini et al., 2006; Velde and Meunier, 2008; Rossi and Graham, 2010; Graham et al., 2010). Rock weathering that implies the dissolution of primary minerals and precipitation/crystallisation of secondary ones changes the bulk chemistry of the rocks (Meunier et al., 2007, Velde and Meunier 2008, Navarre-Sitchler et al., 2009). Chemical weathering is generally dissociated from the physical changes in the rock provoked by weathering. These changes affect rock petrophysical properties (porosity/permeability), which are coupled with the modification of mechanical properties as well (Eppes, 2022). The pore network, its geometry (connectivity of pores and fissures, size of pore apertures), is one of the most important physical characteristics of rocks and regoliths because it provides pathways for water flow and solute transport. Porosity controls the time evolution of mineralogy and weathering. Indeed, the increase in water flow in turn enhances chemical weathering by infiltration of meteoric fluids with dissolved CO_2 and O_2 (and/or organic acids) into large fractures and in microporous zones (microsystems). These fractures may be progressively filled by clay minerals and oxy-hydroxides as

https://doi.org/10.1016/j.geoderma.2022.116247
Received 3 February 2022; Received in revised form 21 October 2022; Accepted 30 October 2022
Available online 16 November 2022

weathering progresses (Meunier et al., 2007, Velde and Meunier 2008, Rossi and Graham, 2010, Graham et al., 2010). Weathering induces changes in pore network geometry, pore apertures and thus rates of fluid transport. This has a controlling effect on long-term rock weathering and soil production (Navarre-Sitchler et al. 2009; 2013; 2015; Hayes et al., 2019). Therefore, a fundamental understanding of how the pore network evolves with increasing weathering and mineral transformations is necessary for predicting long-term weathering in the field as well as mineral dissolution kinetics in the laboratory (White et al., 2002, Navarre-Sitchler and Brantley, 2007).

As pointed out by Eppinger et al. (2021), the proposed contribution should lead to significant progress in the understanding of different kind of processes related to weathering. For example, during the evolution of the landscape, new cracks are created, and existing cracks continue to open, depending on the local orientation of the stress tensor and the topography (Moon et al., 2017; Saint Clair et al., 2015). The size, orientation, and density of cracks in the subsurface adapt to changes in stress state and topography over time. At the scale of the landscape, the knowledge of porosity evolution is one key parameter for predicting water storage capacity and water flow.

Here we present the effect of weathering on the changes in porosity in a thick soil profile of south Brazil developed on a granodiorite basement. The porosity formed during weathering was investigated using both X-ray Computed Tomography (XRCT) and the ^{14}C-PMMA method. The ^{14}C-PMMA method (Hellmuth and Siitari-Kauppi, 1990; Hellmuth et al., 1991, 1993, 1994), allows mapping porosity of a rock section via the pore space impregnation by MethylMethAcrylate doped in ^{14}C, and the subsequent analysis of an autoradiograph of this section. Because fractures/cracks formed during weathering are important to quantify as they are preferential and fast fluid pathways in the rock, controlling its permeability and the accessibility of solutes to interaction sites, an effort was made using these imaging methods for characterising the proportion and aperture distribution of fractures during weathering. A specific imaging method developed by Bonnet et al. (2020) was employed for estimating fracture porosity, aperture and density generated at different weathering stages.

2. Materials and methods

Location, geological setting, and environmental conditions are described in Bonnet et al. (2022). The weathering profile of an average thickness of 20 m is divided into four parts: the un-weathered rock, the saprock of ~2 m thickness with spheroidal weathering, a ~15 m thick saprolite and the soil of ~2 m thickness (Bonnet et al., 2022). The un-weathered rock appears as large boulders of dark grey color in the bottom of the profile underlain by the granodiorite outcrops. The granodiorite contains large phenocrysts of orthoclase (2–3 cm) and equigranular crystals (0.5–1 cm) of quartz, plagioclases, and biotite. The saprock corresponds to the first stage of weathering with preservation of the structure of the un-weathered rock. The mechanical resistance is reduced and in the field the samples are breakable by hand. In the saprolite (or gruss) the cohesion of the un-weathered rock is no longer preserved, and most primary minerals are weathered without changes in their relative positions. In the top of the saprolite remaining un-weathered minerals are no more joined.

The samples are friable and crumbled by hand in the field. The bottom of the saprolite and the saprock contain un-weathered corestones of several dm to m in diameter surrounded by onionskin like structures (spheroidal weathering). The soil, on the top of the weathering profile forms a 2 m thick and clay-rich layer with reddish-ochre colour which is due to the presence of iron oxy-hydroxides. More detailed description is given in Bonnet et al. (2022).

2.1. Bulk density and porosity measurements

The bulk density and porosity were measured on un-weathered rock and saprock samples by immersion into the water according to Flint and Flint (2002). Saprolite and soil samples were too friable to be applied using this method. The samples (several cm^3) were weighted after drying at 110 °C for 48 h to remove all residual water. The samples were placed into the vacuum and progressively immersed into degassed water to fill the porosity with water and stayed immersed for 2–3 weeks to ensure complete saturation of the pores with water. Then the samples were weighed in the saturated state and under immersion in water. This procedure allowed to measure the total volume and subsequently the bulk density (g cm^{-3}) and bulk porosity calculations.

2.2. Porosity characterisation using ^{14}C-PMMA (PolyMethylMethAcrylate) method

To quantify the connected porosity of the rock at different stage of weathering with a spatial resolution of ~20 μm, the samples were impregnated with the ^{14}C-MethylMethAcrylate (MMA) liquid monomer (Siitari-Kauppi, 2002; Oila et al., 2005; Sardini et al., 2006, 2009, 2015; Mazurier et al., 2016; Bonnet et al., 2020; Delayre et al., 2020). The un-weathered rock (GRV01), saprock (GRV03, GRV04) and saprolite (VIA03) samples were dried in a vacuum in an oven set at 50 °C for 11 days to remove all residual water before impregnation. The samples were impregnated into liquid ^{14}C-labelled MethylMethAcrylate (^{14}C-MMA – the activity of 167 kBq mL^{-1} for GRV01, GRV03 and VIA3 and 81 kBq mL^{-1} for sample GRV04), for one month (the University of Helsinki, Department of Chemistry) to allow the impregnation of all connected porosity including microcracks and microporous mineral aggregates. The samples were then irradiated (Scandinavian Clinics Estonia OÜ) with γ rays (^{60}Co source – 100 kGy) to induce the polymerisation of the resin in ^{14}C-PMMA into the pore space. After polymerisation, the samples were cut, carefully polished with silicon carbide powder (600 Mesh) and then diamond abrasive discs to a flat surface. The polished rock sections were then exposed on the autoradiographic film (Kodak BioMax MR®) with a ^{14}C calibration series of ten activities ranging from 462 Bq mL^{-1} to 333 Bq mL^{-1} to obtain a quantitative autoradiograph of the ^{14}C activity. The exposure time was adjusted to reveal both macro- and microcracks and microporous mineral aggregates. A too long exposure time causes film saturation especially for large cracks of wide aperture while, on the contrary, a too short exposure time does not reveal narrow aperture microcracks (Siitari-Kauppi, 2002). In this study, the better compromise for studying all porosity was an exposure time of five days. The autoradiographs were scanned (tabletop Microtek's ArtixScan F1®) with a resolution of 1200 dpi (i.e. pixel of 21.17 μm) in 8 bit (256 grey levels) giving a connected porosity digital map of each studied rock section (Supplementary Fig. 1a) (Oila et al., 2005; Kelokaski et al., 2006; Leskinen et al., 2007; Voutilainen et al., 2012; Robinet et al., 2012; 2015; Bonnet et al., 2020). The detailed procedure is provided by Siitari-Kauppi (2002). The grey level of each pixel of the film was converted to an optical density (OD) using the calibration series, and then into activity using Keller and Waser (1982) approach. The activity of each pixel was normalized by the activity of the pure resin A_0 (Siitari-Kauppi, 2002). The porosity is calculated for all the pixels of the digitized map and bulk porosity is comparable to values obtained by water saturation (Siitari-Kauppi, 2002) or X-ray computed tomography (Mazurier et al., 2016; Robin et al., 2016, Robinet et al. 2015). The exact expression used for converting activity to porosity can be found for instance in Robinet et al. (2015). The spatial resolution of the ^{14}C PMMA method is about 20 μm. However, connected microcracks with a small aperture (<1 μm) are also revealed because they appear as a continuous line of a point source in the autoradiograph (Sardini et al., 2014; Bonnet et al., 2020).

2.3. Porosity characterisation using X-ray Computed microtomography (XRCT)

The study of pore space of rocks and soils using XRCT has become

more and more popular for two decades (Cnudde and Boone, 2013; Fusseis et al., 2014; Robinet et al., 2012, 2015; Voutilainen et al., 2012; Arns et al., 2004; Mazurier et al., 2016; Schlüter et al., 2021; Puche et al., 2022). The images of pore structure obtained by XRCT differs from the ones obtained by the ^{14}C-PMMA method. First, XRCT provides a 3D representation of the material, whereas the ^{14}C-PMMA is 2D. Second, XRCT is a completely non-destructive method, whereas the ^{14}C-PMMA method is semi-destructive because the pore space is filled with resin. Third, the local intensities estimated on the XRCT images are a function of the local attenuation coefficients of the material by X-ray (they are not directly a function of the porosity), whereas intensities measured in images resulting from the ^{14}C-PMMA method are a linear function of the porosity. On XRCT images, at first glance, pores appear in black because pores are filled with air or resin, having a low attenuation coefficient compared to minerals. However, if the pore size is lower than voxel size, the intensity is a function of porosity and mineral content and nature. Then porosity can be also obtained from XRCT by processing the image (Ketcham and Carlson, 2001). However, the resolution should be sufficient (or in another word small voxel size is needed) to apply this technique, which represents a strong limitation if the sample size is pluricentimetric.

In the present study, we decided to use XRCT because it is complementary to the ^{14}C-PMMA method and non-destructive. Samples were scanned with a X-ray micro-tomograph (XRμCT) (EasyTom XL Duo, RX-Solutions, France). The micro-tomographic acquisition was done in staking mode with 4320 projections distributed over 3 turns to scan each whole sample (GRV01, GRV03, VIA03). A micro-focus source (Hamamatsu L12161) set at a voltage of 140 kV and a tube current of 180 μA was used, coupled to a flat panel detector (Varian PaxScan 2520 DX; 1920x1536 matrix pixel; pixel pitch of 127 μm; 16 bits of dynamics) with frame rate of 12.5 fps and an average of 14 images (i.e., total exposure time of 1.12 s per projection). The source object distance and the source detector distance were 147 mm and 374 mm, respectively. A copper filter of 0.35 mm thickness was used to reduce beam hardening effects. An anti-ring procedure with random shifts of the detector have been used. The reconstruction was done with the XAct 10251 v1.1 software (Rx-Solutions, France) with a filtered back projection algorithm (Feldkamp method-cone beam geometry with Tukey filter and a sinus apodization filter). Beam hardening artefacts have been corrected through linearization with a polynomial function. The results are three sets of 16-bit cross sections with a voxel resolution of 49.94 μm.

2.4. Pore aperture quantification

2.4.1. Cracks detection

To represent the crack network of the samples, the segmentation of the cracks (i.e. their detection) is crucial because their apertures may vary as a function of the degree of weathering and for the different minerals. Generally, two types of cracks are observed and based on their aperture: cracks with apertures < 50 μm were referred to as microcracks, and cracks with apertures ≥ 50 μm were referred to as macrocracks (Mazurier et al., 2016, Bonnet et al., 2020). This empirical distinction

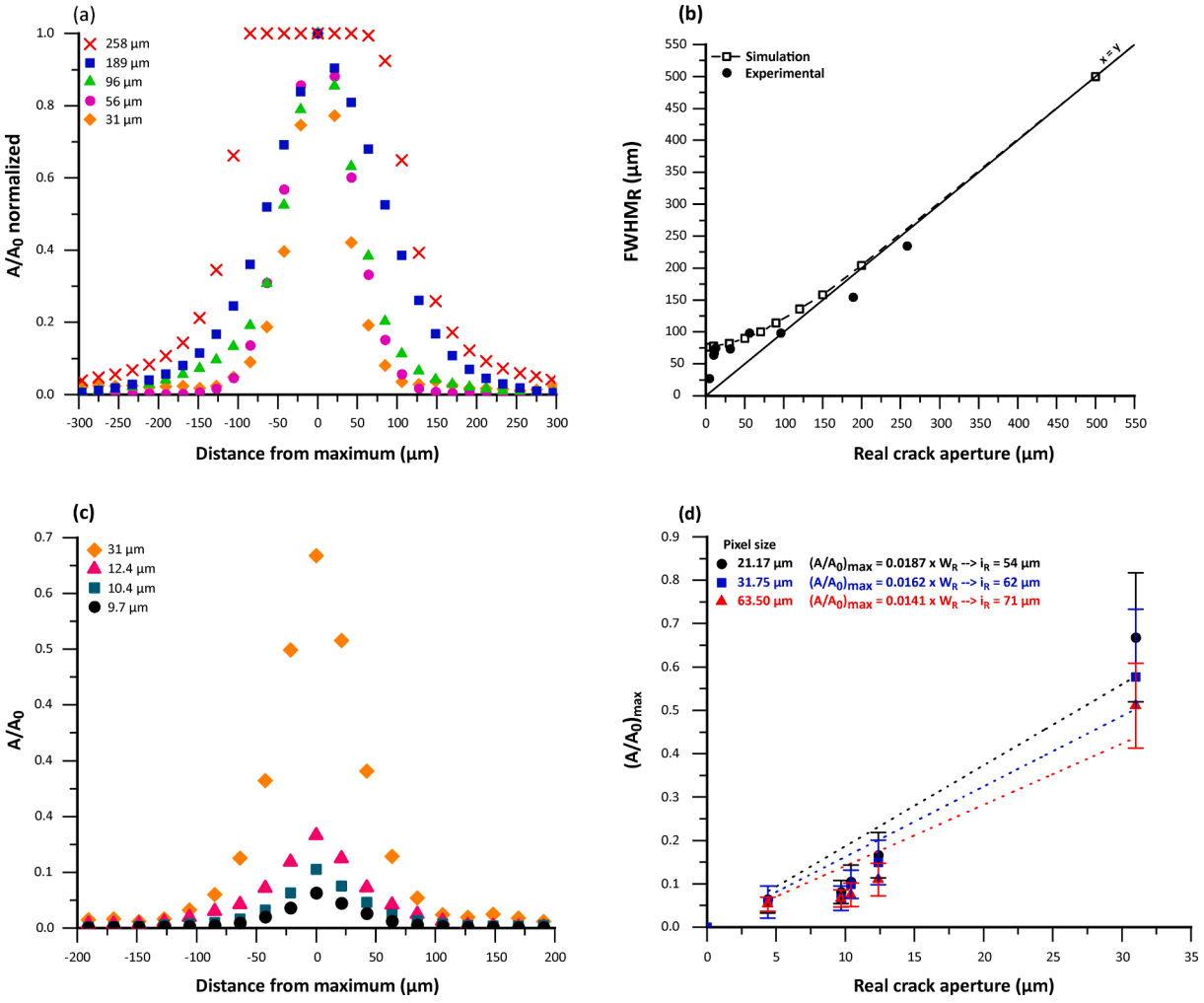

Fig. 1. Activity profile of macrocracks (a) and the use of FWHM to determine their aperture (b). Activity profile of microcracks (c), and (d) change in maximum of normalized activity $(A/A_0)_{max}$ according to real crack apertures. All of these fractures are here perpendicular to the autoradiographic plan.

was made because of their specific profiles obtained by autoradiograph (Kuva et al., 2015) and water behaviour in soils (Brewer, 1976; Luxmoore, 1981; Beven and Germann, 1982; Rossi and Graham, 2010 and cited references).

On autoradiographs, macrocracks exhibit thick activity profiles with variable Full Width at Half Maximum (FWHM) and high activity ($A/A_0 \sim 1$) (almost maximum film blackening) (Fig. 1 and Supplementary Fig. 1). Microcracks have thinner profiles with little variation in width (FWHM) and variable activity (A/A_0) at their center (variable film blackening) (Fig. 1 and Supplementary Fig. 1). Macrocracks and microcracks are thus dissociated from each other according to the activity value (A/A_0) at their medial axis. An increase in the FWHM associated with $A/A_0 \sim 1$ indicates macrocracks. Low activity at the medial axis ($A/A0 \ll 1$) indicates microcrack. This dissociation was validated by simulations of the autoradiographic process, and the manufacturing of artificial crack samples using glass plates (Sardini et al., 2014; Kuva et al., 2015; Bonnet et al., 2020).

On XRCT or ^{14}C-PMMA autoradiographic images, the grey level at the medial axis of macrocracks represents the X-ray absorption coefficients of the pure PMMA, and the activity of the pure resin (A0), respectively. Thus, such macrocracks can be easily detected by simple thresholding by boundary. Contrary to the ^{14}C-PMMA method, microcracks are less obvious to detect (Mazurier et al., 2016) using XRCT. It is commonly considered that the sensitivity of XRCT allows crack detection if the crack aperture is higher than around one-tenth of the voxel size. Thus, a significant amount of microcracks is not detected using XRCT. The methodology used to detect cracks is based on mathematical morphology tools (Soille, 2004) with Micromorph™, Aphelion®, and ImageJ® softwares used by Mazurier et al. (2016) and Bonnet et al. (2020). The method, described by Mazurier et al. (2016), provides the medial axis (skeleton) of the microcracks, and the final result is the skeletonized image of microcracks, meaning that one-pixel thick line represents a microcrack (Fig. 2). The skeleton image superimposed to the initial image is shown in Fig. 2 and Supplementary Fig. 1.

2.4.2. Fracture density

From the image of the skeletonized cracks, it was possible to calculate fracture density (D, mm^{-1}) that corresponds to the number of pixels forming a crack (N) multiplied by the size of the pixel (L, mm) divided by the total surface area of the image (A, mm^2) (Mazurier et al., 2016) as follows (eq. (1)).

$$D = \frac{(N \times L)}{A} \tag{1}$$

Fracture density was subsequently calculated for microcracks (μ) and macrocracks (M). To perform that, it was necessary to skeletonize the macrocrack network to determine the number of pixels forming the crack (N_M) using the following equation (eq.2).

$$D_M = \frac{(N_M \times L)}{A} \quad ; \quad D_\mu = \frac{(N_\mu \times L)}{A} \tag{2}$$

With N_M and Nμ the number of pixels constituting the macrocracks and microcracks network, respectively.

Calculating the density of cracks makes it possible to understand how the pore network of a rock sample evolves with the degree of weathering.

2.4.3. Fracture apertures

In this work we used the method proposed by Bonnet et al. (2020) to quantify the distribution of crack apertures. The crack apparent apertures estimated here are the apertures measured in the observation section. The apparent aperture of macrocracks was estimated using the

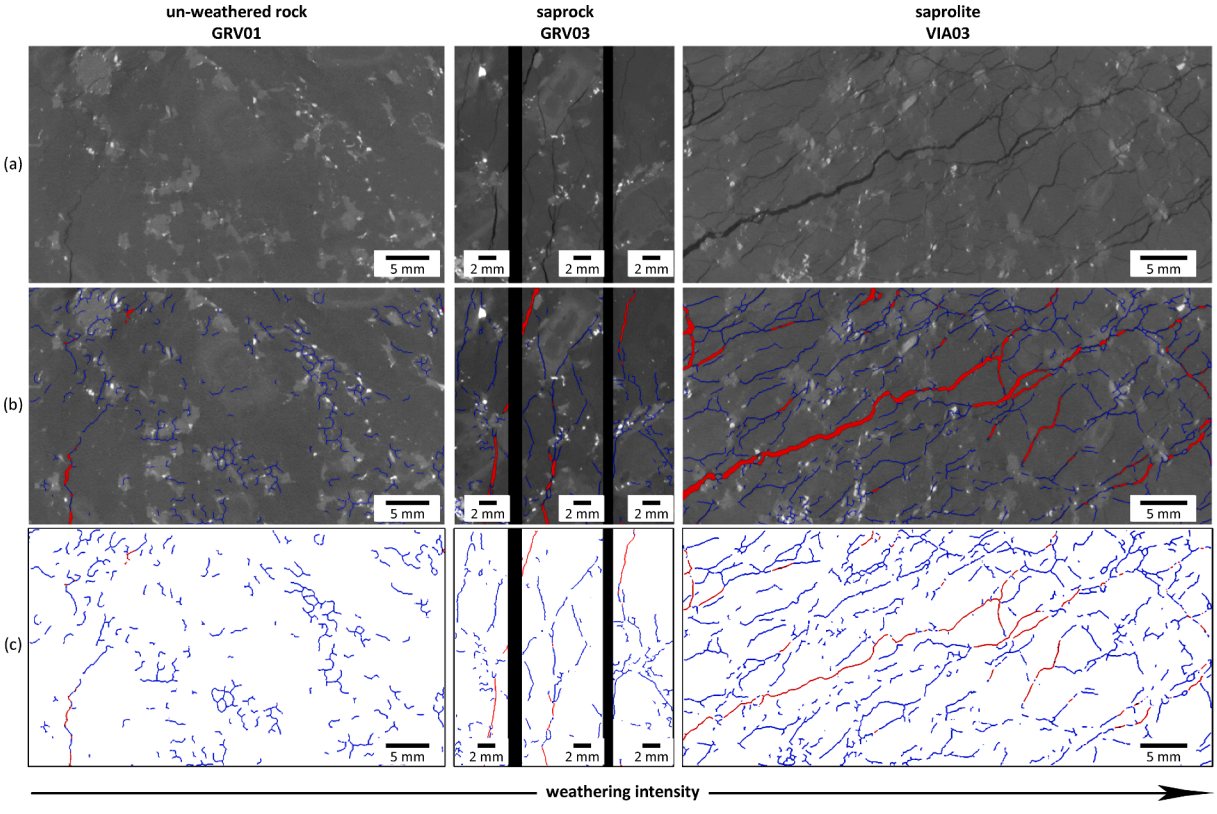

Fig. 2. (a) X-ray microtomographic images of un-weathered rock (GRV01; left), saprock (GRV03; centre) and saprolite (VIA03; right). (b) Crack segmentation for the calculation of porosity (total, macro-, and microcracks): macrocracks appear in red and microcracks (skeletons) appear in blue. (c) Skeletonization of macrocracks for the calculation of crack density (total, macro-, and microcracks). (voxel size = 50 μm). (For interpretation of the references to color in this figure legend, the reader is referred to the web version of this article.)

Full Width at Half Maximum (FWHM) of their activity profile (Fig. 1 and Supplementary Fig. 1, Bonnet et al., 2020). In practice, the aperture distribution of macrocracks was obtained by a granulometry by opening (Coster and Chermant, 1989). The apertures of microcracks were estimated using the procedure described by Mazurier et al. (2016) to obtain their skeleton as described in the supplementary information. The grey levels of the skeletonized microcracks were converted into apparent apertures using their activities deduced from the calibration of grey levels. The apparent aperture of the microcracks was estimated using the maximum normalized activity that is a linear function of crack aperture (Fig. 1 and Supplementary Fig. 1, Bonnet et al., 2020; equation (3)). This approach was tested by analysing activity profiles of artificial crack samples and was also validated and generalized to tilted cracks using the simulation of activity profiles and different pixel sizes of the digitalized autoradiography (Bonnet et al., 2020). The apparent apertures (w_A) were obtained from their maximum normalized activity value $(A/A_0)_{max}$ using the linear relation determined by Bonnet et al. (2020, eq. (3)).

$$w_A = i_R \times \left(\frac{A}{A_0}\right)_{max} \quad (3)$$

w_A is the apparent crack aperture in μm and i_R (μm) is a linear fit parameter ($i_R = 1/\text{slope} = 70$ μm).

The combination of water saturation/immersion, XRCT and especially autoradiography allows a multiscale quantitative description of the porosity and the determination of the apparent aperture of the cracks from <1 μm to >1 mm. Total fracture porosity can be also estimated by the sum of the contribution of micro and macrocracks porosity [eq. (4)]. Fracture porosity is obtained by multiplying fracture density and average fracture aperture. The total fracture porosity Φ_f is:

$$\Phi_f = D_M\overline{w_M} + D_\mu\overline{w_\mu} \quad (4)$$

The determination of analytical errors on crack apertures has not yet been studied. The analytical errors on apertures result from three successive calculations: optical densities, activities, and apertures (Sammartino et al., 2002). The main source of error comes from the calculation of the optical densities, which causes a relative error of >100 % for a crack opening of less than 1 μm. The relative errors on the aperture vary from 50 % to 60 % for apertures ranging from 20 μm to 5 μm respectively. More detailed explanations are given in supplementary information.

Table 1
Porosity and density measurements obtained by water immersion method.

Morphological unit	Sample	Total porosity Φ (%)	Bulk density ρb (g.cm^{-3})	Grain density ρg (g.cm^{-3})
Rock	GRV01	1.73 ± 0.01	2.66 ± 0.01	2.71 ± 0.03
Saprock	GRV03	3.57 ± 0.01	2.58 ± 0.02	2.68 ± 0.02
	GRV04	5.47 ± 0.01	2.54 ± 0.02	2.69 ± 0.02
	GRV05	10.54 ± 0.01	2.41 ± 0.02	2.69 ± 0.02
Saprolite	VIA02	11.02 ± 0.01	2.40 ± 0.02	2.70 ± 0.01

3. Results

3.1. Water saturation/immersion

The water saturation/immersion estimates the total connected porosity of the samples obtained from bulk and dry density measurements (Table 1). The un-weathered granodiorite has a mean total porosity of 1.73 % that falls in the typical range of porosity for fresh granitic rocks (Rossi and Graham, 2010; Mazurier et al. 2016). The total porosity increases upward in the saprock from 3.57 % to 10.5 % due to an increase in physical fragmentation and chemical weathering (Bonnet et al., 2022). The increase is progressive with weathering of biotite and increases sharply with the weathering of feldspars. Total porosity reaches 11 % at the top of the saprolite. The bulk density decreases from 2.66 kg dm^{-3} in the un-weathered rock to 2.40 kg dm^{-3} in the top of the saprolite. The quite high values of bulk densities measured for saprolite samples may be related to the fact that the analysed profile presents low chemical weathering intensity (Bonnet et al., 2022). The grain density remains similar in all the layers (2.68–2.71 kg dm^{-3}). Bulk densities of the topsoil were not determined.

3.2. XRCT

The total porosity obtained by XRCT after segmentation for the un-weathered rock is 1.29 % (Table 2). This lower value than that obtained with the water saturation method is most probably due to the resolution of XRCT not allowing the detection of all the microcracks (Fig. 2). The porosity increases from 2.50 % in the saprock to 4.39 % in the saprolite (Table 2). XRCT allows in addition to differentiate microcracks (aperture < 50 μm) from macrocracks (aperture > 50 μm) and their densities. The differences observed with the immersion method are related to the fact that XRCT does not detect all the microcracks due to the resolution of the method (Mazurier et al., 2016) The total crack density increases from 0.24 mm^{-1} for un-weathered rock to 0.34 mm^{-1} for saprock and 0.48 mm^{-1} for saprolite in relation to the increase in porosity (Table 2) indicating an increase in the number of pores. In general, microcracks are dominant in the un-weathered granodiorite, the saprock and the bottom of saprolite (Fig. 2, Table 2). The densities of microcracks and macrocracks both increase during weathering, with microcracks outnumbering macrocracks (Fig. 2, Table 2). Although the density of macrocracks is lower compared to that of microcracks in the saprolite, the macrocracks contribute most to total porosity (2.27 % vs 2.12 %). The density of macrocracks is almost stable between the saprock and the saprolite (0.05 mm^{-1} to 0.06 mm^{-1}, respectively) but their contribution to total porosity significantly increases (1.06 % to 2.27 %, respectively). This implies a major increase in the aperture of cracks from saprock to saprolite (Figs. 2 and 4) to form macrocracks.

3.3. Autoradiography by ^{14}C-PMMA method

The ^{14}C-PMMA autoradiographic method was used only on the un-weathered rock and one sample of the saprolite (Fig. 3, Table 2). After segmentation and their skeletonization, all cracks were superimposed to the autoradiographic image (Fig. 3). The skeleton of all kinds of cracks is

Table 2
Porosity and crack density obtained by XRCT (*) with voxel size of 50 μm or autoradiography ($^{\#}$) with pixel size of 21.7 μm.

	Sample	Rock GRV01		Saprock GRV03	Saprolite VIA03	
Porosity Φ (%)	Total porosity	1.29*	1.66$^{\#}$	2.50*	4.39*	11.71$^{\#}$
	Microcracks porosity	1.14*	1.45$^{\#}$	1.44*	2.12*	2.61$^{\#}$
	Connected microporosity		0.03$^{\#}$			0.09$^{\#}$
	Macrocracks porosity	0.15*	0.18$^{\#}$	1.06*	2.27*	9.01$^{\#}$
Cracks density (mm^{-1})	Microcracks density	0.23*	0.25$^{\#}$	0.29*	0.42*	0.36$^{\#}$
	Macrocracks density	0.01*	0.03$^{\#}$	0.05*	0.06*	0.58$^{\#}$
	Total crack density	0.24*	0.28$^{\#}$	0.34*	0.48*	0.94$^{\#}$

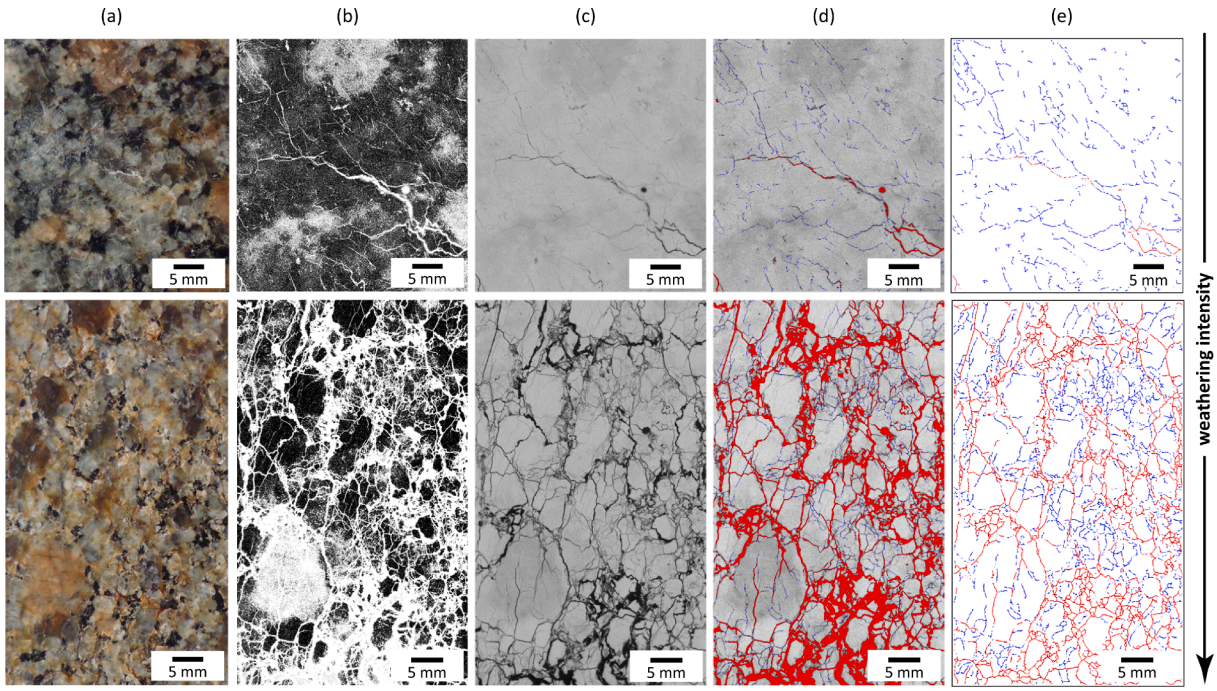

Fig. 3. A) photographs of un-weathered rock (GRV01; top) and saprolite (VIA03; bottom); b) corresponding porosity images (porosity appears in white); c) corresponding autoradiographs (8 bits) (cracks appear in dark); d) crack segmentation for the calculation of porosity (total, macrocracks, microcracks, microporosity): macrocracks appear in red and microcracks (skeletons) appear in blue and microporous minerals in greyscale; e) Skeletonization of macrocracks for the calculation of crack density (total, macrocracks, microcracks). (pixel size = 21.17 μm; exposure time = 8 h). (For interpretation of the references to color in this figure legend, the reader is referred to the web version of this article.)

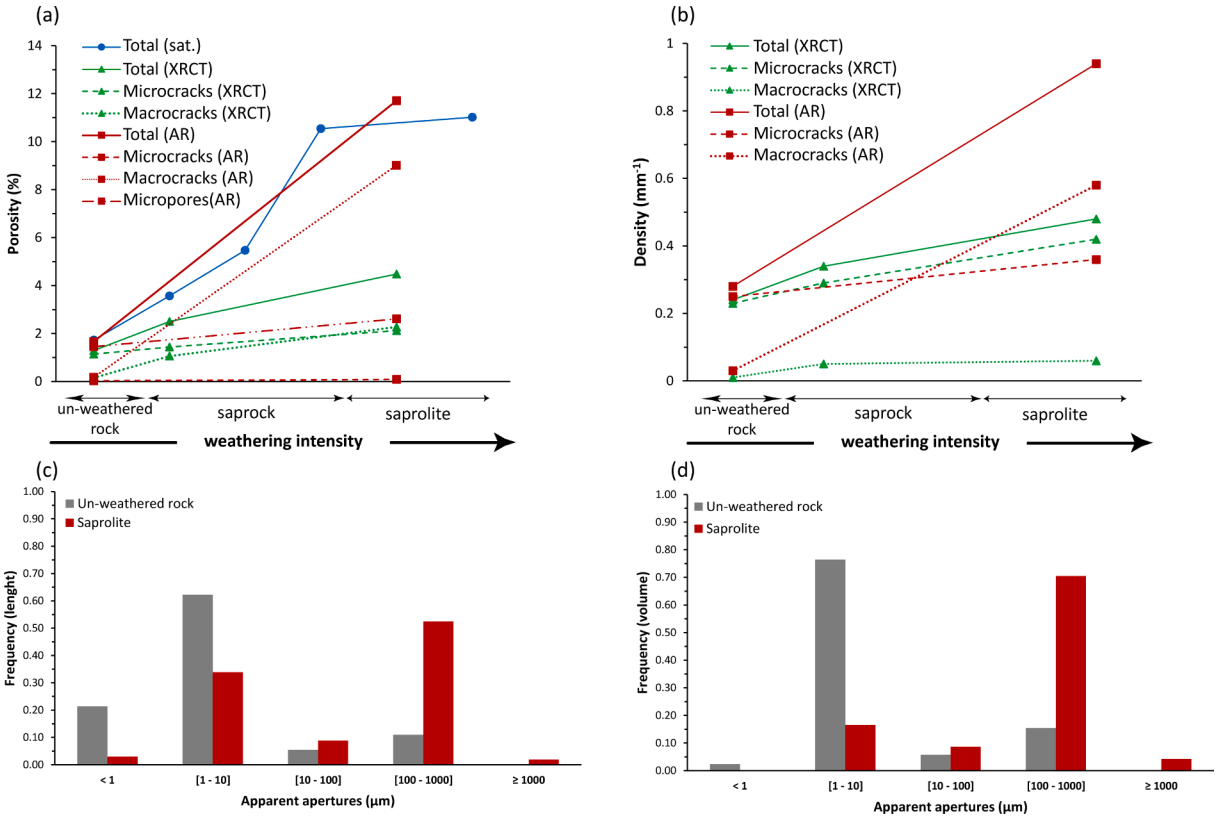

Fig. 4. Evolution of total porosity (a), crack density (b) and apparent crack opening ((c) by length, (d) by volume) during weathering. (Sat = water saturation method; MT = X-ray microtomography method; AR = ^{14}C-PMMA method).

only used to measure their density. The total connected porosity increases from 1.66 % in the un-weathered rock to 11.71 % for the saprolite (VIA03) (Figs. 3 and 4, Table 2). The values obtained by water immersion and autoradiography are close indicating the same pores are measured by immersion in water or MMA. The fact that total porosity measured by the ^{14}C-PMMA autoradiographic method is higher than that measured by XRCT is attributed to the heterogeneity of the rock as two different samples were used and, also because some microcracks and all micropores are not considered by XRCT.

The connected porosity related to microcracks increases from 1.45 % in the un-weathered rock to 2.61 % in the saprolite whereas the porosity related to macrocracks increases more largely from 0.18 % to 9.01 % respectively (Figs. 3 and 4, Table 2). The connected microporosity is the one that contributes less to the total porosity in the un-weathered rock (0.03 % out of 1.66 %). Although connected microporosity value increases in saprolite (0.09 % out of 11.71 %), it is no longer the major contribution to the total connected porosity of the rock (Fig. 4, Table 2). Thus, in the un-weathered rock, intragranular microcracks in biotites, plagioclases, and K-feldspars are the main contributors; whereas in the saprolite sample, connected macrocracks are the main contributors to the porosity (Fig. 3). Autoradiography also reveals that with increasing weathering, microporous mineral grains are mainly located in plagioclases and K-feldspars, as shown by grey areas on the autoradiographs (Fig. 3 c-d) or in white in the porosity image (Fig. 3b). This porosity contributes to the microporosity which is not detected by petrographic observations or XRCT. This microporosity is attributed to incipient weathering and pseudomorphic replacement by clay minerals such as kaolinite (Bonnet et al., 2022).

In relation to weathering, total crack density increases from 0.28 mm^{-1} to 0.94 mm^{-1} for un-weathered rock and saprolite, respectively (Table 2). The density of microcracks increases with weathering from 0.25 mm^{-1} for un-weathered rock to 0.36 mm^{-1} and for saprolite. Although the density of microcracks outnumbers that of macrocracks in the un-weathered rock, they do not contribute most to the connected porosity because the aperture of the less numerous macrocracks is large enough to be the major contributor to total porosity (Fig. 4, Table 2). The density of macrocracks increases more significantly from 0.03 mm^{-1} to 0.58 mm^{-1} from un-weathered rock to saprolite.

The average aperture of the microcracks determined by autoradiography is about 2.4 ± 1.2 μm in the un-weathered rock and 3.89 ± 2

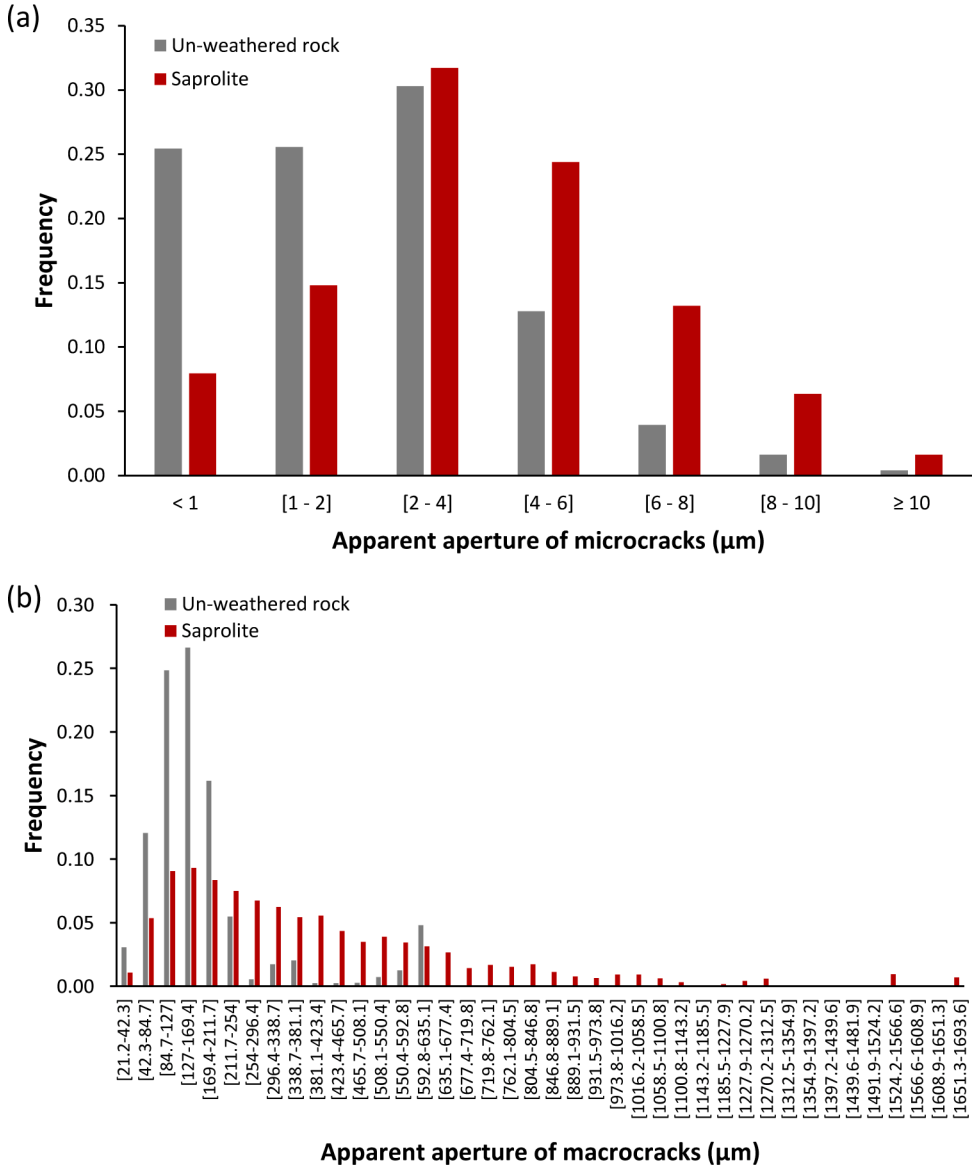

Fig. 5. Distribution of the aperture of (a) microcracks and (b) macrocracks of un-weathered rock (GRV01) and saprolite (VIA03) obtained by autoradiography (pixel size = 21.17 μm; exposure time = 8 h).

μm in the saprolite. The opening of the macrocracks evolves from 176 μm in the un-weathered rock to ~ 400 μm in the saprolite. Fig. 5 shows the distribution of crack apertures. The distribution is significantly different for the two weathering stages. Un-weathered rock has microcracks with an opening mainly from<1 μm to about 6 μm and macrocracks with between 40 μm and 250 μm, whereas saprolite has microcracks with an opening between 1 μm and 8 μm and macrocracks ranging between 40 μm and 900 μm (Fig. 5). These features clearly indicate an increase in the apertures of the cracks related to the weathering intensity estimated by element losses and silt and clay formation (Bonnet et al., 2022). The results highlight that the connected microcracks of un-weathered rock contribute mainly to the total connected porosity and are the precursor of fracture enlargement during weathering. This quantification of the aperture is very important to understand the simultaneous changes of rock permeability with weathering.

4. Discussion

The detailed study of weathering presented herein depicts the change in rock fabric (and especially cracking) according to weathering intensity.

The total porosity of un-weathered rock estimated to be 1.29 % or 1.66 % by microtomography and ^{14}C-PMMA autoradiography, respectively, corresponds to a poorly developed connected network of intergranular microcracks: a few thin cracks localized at the cleavage of biotites, within plagioclases, K-feldspars or at grain boundaries were found (Fig. 3 a-e). Although intergranular macropores are few compared to microcracks, their larger opening (~176 μm vs ~ 2.4 μm) allow them to contribute significantly to the total porosity of the rock (Figs. 2 and 3, Table 2). The microcracking without changing the relative position of mineral grains in un-weathered rock could be related to rock shrinkage during its cooling, decompression during its exhumation towards the surface, and possible early mineral transformations such as biotite expansion during hydrothermal alteration or incipient weathering (Wahrhaftig, 2015). Microfractures are formed when the stress experienced by the rock is higher than its local strength. Moreover, according to the geological map of the region, tectonic events could have faulted the outcrop. The concept of subcritical cracking (Eppes, 2022; Eppes and Keanini, 2017) is well adapted to describe the slow cracking of rocks during weathering caused by combined chemo-mechanical processes. For instance, cracks observed in un-weathered rock could be growth subcritically during the cooling of the granite, whereas cracks observed in the weathered granite have also grown subcritically but during chemical weathering. These cracks are tensile cracks because, supporting by the fact that shear along cracks has not been clearly observed. An important aspect of the proposed contribution is to quantify crack openings, a component of crack size that is rarely analysed. The observed progressive opening of existing cracks and the generation of new cracks during weathering is caused by subcritical cracking.

The results of microtomography and ^{14}C-PMMA method showed an increase in crack density and aperture of both microcracks (~2.5 μm) and macrocracks (396 μm) with weathering. Autoradiography revealed that the density of macrocracks becomes the same order of magnitude as that of microcracks mainly responsible for the increase of the total porosity to ~ 11 % in the saprolite. Accordingly, the pore network develops by the formation of new intragranular and intergranular cracks (crack density is ~ 3 times higher), but porosity mainly increases by the increase of the aperture of cracks already present in un-weathered rock (Figs. 2 and 3). The macrocracks develop by the expansion in biotites and the dissolution pits in feldspars, mainly plagioclases and to a lesser extent K-feldspars, that increase with chemical weathering degree (Bonnet et al., 2022). Microtomography shows in addition that at a certain stage of weathering, the density of macrocracks is stable but their associated porosity continues to increase (Fig. 2, Table 2) because their apertures and connectivity are more important as also shown by autoradiography (Fig. 3, Table 2) and SEM (see Bonnet et al., 2022). Mazurier et al. (2016) have shown that the total density of the cracks did not change significantly with the degree of weathering but that their opening did imply changes in the proportion of the porosity associated with these two categories of pores. We did not observe this behaviour with a simultaneous increase in both density and aperture with the degree of weathering (Fig. 4). However, the present study is limited to two samples and Mazurier et al. (2016) studied rock with a minor chemical alteration.

The concomitant increase of connected pore space and pore size induces a large increase of hydraulic conductivity allowing advective transport of weathering fluids and products and consequently weathering rates (Lebedeva et al., 2010; Maher and Chamberlain, 2014, Gu et al., 2020). In the top of the saprolite, the samples present a very open pore network with rare contacts between minerals grains (GRV09) and therefore abundant macrocracks (GRV10).

The porosity of the un-weathered rock at the bottom of the profile can be considered as the parent porosity of the rock before weathering. This porosity is assumed to be equivalent for all the protolith whatever its relative position in the weathering profile (saprock, saprolite, soil). The porosity created by weathering is assumed to induce the difference in porosity values between the un-weathered rock and the saprolite (Navarre-Sitchler et al., 2013; Bazilevskaya et al, 2013, 2015). Between the two stages, the total porosity is 7 times higher (from 1.66 to 11.71 %), the microcracks density almost doubled (1.45 to 2.61 mm^{-1}), while the macroporosity was 50 times higher (0.18 to 9.01 %). The proportion of porous minerals was threefold (0.03 to 0.09 %). Petrographic observations during weathering (Figs. 6–9, Bonnet et al., 2022) also show that the pore network develops more rapidly once the feldspars weather, explaining the rapid increase of pore apertures with increasing weathering in the saprolite.

These results highlight the pre-existing pores of the un-weathered rocks plays a key role in the initiation of the weathering by permitting weathering fluids. The first mineral to weather is biotite by progressive transformation into vermiculite in the saprock and then into smectite in the saprolite (Bonnet et al. 2022) and the initial porosity development in the granodiorite is caused by the fracturing along cleavages that creates microcracks network.

This allows weathering fluids infiltration and dissolution of other minerals such as plagioclase (Bazilevskaya et al., 2013, 2015). When plagioclases weather, porosity and especially macrocracks increase significantly. The development of the network of microcracks and then macrocracks is responsible for the progression of the weathering. When only microcracks and microporous minerals (revealed by autoradiography – Fig. 3 bottom) are present, the incipient weathering occurs at the scale of contact weathering microsystems (few μm) (Meunier et al., 2007; Ballesteros et al., 2010). In the micro- to nanopores (grain joints and cleavages), the resident (non-circulating) fluids are close to chemical equilibrium; weathering processes are controlled by the diffusion of the elements (diffusion-limited dissolution - Navarre-Sitchler et al., 2013, Meunier et al., 2007; Velde and Meunier 2008). The driving force of mineral weathering is linked to the contrasts of chemical compositions of the parent minerals compared to that of the fluids which impose local gradients of chemical potentials. As long as the formation of macrocracks is not too important, the structure of the initial rock is preserved, and the weathering is controlled by diffusion processes. During the weathering of plagioclases and coalescence of dissolution pits in the saprolite, the weathering is driven by advection processes with circulating fluids in macrocracks. In the macrocracks, the circulating fluids are far from chemical equilibrium due to larger and faster dilution by meteoric water. The weathering systems are more open and correspond to the fissure microsystems (Meunier et al., 2007; Ballesteros et al., 2010). The opening of the porosity during granodiorite weathering also allows the storage of water (available water, water holding) and water flow. Weathering form clay minerals and iron oxides crystallize in the porosity and partly fill it (Figs. 6–9, Bonnet et al., 2022).

The proportion of filled porosity tends to increase with chemical weathering but is difficult to estimate. The inferred reactive surface area is lower than the specific surface area measured by gas absorption methods for example (Hochella and Banfield, 1995; Helgeson et al., 1984; White and Peterson, 1990; Drever and Clow, 1995; Brantley and Mellott, 2000, White et al. 2002, 2003, Putnis, 2002, 2009; 2015, Merino et al., 1993, Jamtveit et al., 2009, 2011). In addition to the quantification of crack aperture through 4–5 decades (< μm to cm), the ^{14}C-PMMA autoradiography reveals the filling of the pore by secondary minerals. The filled pores appear with different grey levels from the unweathered minerals (non-porous) and the empty pores (Figs. 6–9, Bonnet et al., 2022). However, in this profile the sealing of porosity was not too effective as only 5 % of clay sized particles are formed in the top saprolite. At the scale of weathering microsystems (or mineral aggregates), autoradiography could be tested to estimate the degree of pore filling by secondary mineral and by inference the proportion of mineral surface in the pores that are 'accessible' and not filled by secondary minerals. In addition, the autoradiography method improves the understanding of the processes of porosity development and opening of the microcracks into macrocracks.

5. Conclusion

The surface weathering of crystalline rocks involves mineral and physical transformations that are coupled. The present contribution, associated with the companion paper (Bonnet et al. 2022), presents jointly and in a detailed way the two consequences of weathering. The coupling of these transformations is approached qualitatively and allows us to describe in detail the transformations affecting the Viamão granodiorite, transformations affecting a profile thickness of 15 m. This approach is used to explain the mineral changes related to texture/porosity modifications and could be used to characterize the water storage potential of subsurface aquifers (porosity/hydraulic conductivity) and to characterize the changes in mechanical properties of rocks with weathering. The ability to decipher crack opening (at multiple scales) represents a key development, allowing a better understanding of the change in rock permeability during weathering.

Declaration of Competing Interest

The authors declare the following financial interests/personal relationships which may be considered as potential competing interests: CANER Laurent, BONNET Marine reports financial support was provided by Université de Poitiers. BONNET Marine reports financial support was provided by Région Nouvelle Aqutaine.

Data availability

Data will be made available on request.

Acknowledgments

The authors acknowledge financial support from the European Union (ERDF) and "Région Nouvelle Aquitaine". The authors acknowledge financial support the European Commission under the Industry and Academic Partnership and Pathways–Marie Curie–project "POSINAM" (pore space investigation in natural and artificial materials, 2009–2013, project ID 230635). The authors acknowledge the Department of Geosciences-Instituto de Geociências from the Universidade Federal do Rio Grande do Sul, Brazil for assistance during field work and sampling.

Appendix A. Supplementary data

Supplementary data to this article can be found online at https://doi.org/10.1016/j.geoderma.2022.116247.

References

Arns, C.H., Knackstedt, M.A., Pinczewski, V.W., Martys, N.S., 2004. Virtual permeametry on microtomographic images. J. Petroleum Sci. Eng. 45, 41–46. https://doi.org/10.1016/j.petrol.2004.05.001.

Ballesteros, M., Cantano Martín, E., García Talegón, J., 2010. Role of porosity in rock weathering processes: a theoretical approach. Cuadernos Laboratoiro Xeoloxico de Laxe 35, 147–162.

Bazilevskaya, E., Lebdeva, M., Pavich, M., Rother, G., Parkinson D., Cole D., Brantley S. L., 2013. Where fast weathering creates thin regoliths and slow weathering creates thick regoliths. Earth Surf. Processes Landforms. doi: 10.1002/esp.3369.

Bazilevskaya, E., Rother, G., Mildner, D.F.R., Pavich, M., Cole, D., Bhatt, M., Jin, L., Steefel, C.I., Brantley, S.L., 2015. How Oxidation and Dissolution in Diabase and Granite Control Porosity during Weathering. Soil Sci. Soc. Am. J. 79, 55–73. https://doi.org/10.2136/sssaj2014.04.0135.

Beven, K., Germann, P., 1982. Macropores and water flow in soils. Water Resour. Res. 18, 1311–1325.

Bonnet, M., Sardini, P., Billon, S., Siitari-Kauppi, M., Kuva, J., Fonteneau, L., Caner, L., 2020. Determining crack apertures distribution in rocks using 14C-PMMA autoradiographic method: experiments and simulations. J. Geophys. Res. Solid Earth 124. https://doi.org/10.1029/2019JB018241.

Bonnet, M., Caner, L., Siitari-Kauppi, M., Mazurier, A., Mexias, A.S., Dani, N., Sardini, P., 2022. Weathering of Viamão granodiorite, south Brazil: Part 1 – clay mineral formation and increase in total porosity. Geoderma. https://doi.org/10.1016/j.geoderma.2022.115968.

Brantley, S.L., Mellott, N.P., 2000. Surface area and porosity of primary silicate minerals. Am. Mineral. 85, 1767–1783.

Brewer, R., 1976. Fabric and Mineral Analysis of Soils. Robert E. Krieger Publ. Co., Huntington, NY.

Cnudde, V., Boone, M.N., 2013. High-resolution Xray computed tomography in geosciences: a review of the current technology and applications. Earth- Sci. Rev. 123, 1–17. https://doi.org/10.1016/j.

Coster, M., Chermant, J.-L., 1989. Précis d'Analyse d'images. Presses du CNRS, 560p.

Delayre, C., Sammaljärvi, J., Billon, S., Muuri, E., Sardini, P., Siitari-Kauppi, M., 2020. Comparison of phosphor screen autoradiography and micropattern gas detector based autoradiography for the porosity of altered rocks. Sci. Rep. 10, 9455. https://doi.org/10.1038/s41598-020-65791-7.

Drever, J.I., Clow, D.W., 1995. Weathering rates in catchments. Rev. Mineral. 31, 463–481.

Eppes, M.-C., Keanini, R., 2017. Mechanical weathering and rock erosion by climate-dependent subcritical cracking. Rev. Geophys. 55 https://doi.org/10.1002/2017RG000557.

Eppes, M.-C., 2022. Mechanical Weathering: A Conceptual Overview. In: Shroder, J.J.F. (Ed.), Treatise on Geomorphology, vol. 3. Elsevier, Academic Press, pp. 30–45. doi: 10.1016/B978-0-12-818234-5.00200-5.

Eppinger, B.J., Hayes, J.L., Carr, B.J., Moon, S., Cosans, C.L., Holbrook, W.S., Harman, C. J., Plante, Z.T., 2021. Quantifying depth dependent seismic anisotropy in the critical zone enhanced by weathering of a Piedmont schist. J. Geophys. Res. Earth Surf. 126 https://doi.org/10.1029/2021JF006289.

Flint, L.E., Flint, A.L. 2002. Porosity, in: Dane, J.H., Topp, G.C. (Eds.), Methods of Soil Analysis: Part 4 Physical Methods. SSSA Book Series, 5.4, Soil Science Society of America, Madison, WI, pp. 241–254.

Fusseis, F., Xiao, X., Schrank, C., De Carlo, F., 2014. A brief guide to synchrotron radiation–based microtomography in (structural) geology and rock mechanics. J. Struct. Geol. 1–16 https://doi.org/10.1016/j.jsg.2014.02.005.

Graham, R.C., Rossi, A.M., Hubbert, K.R., 2010. Rock to regolith conversion: producing hospitable substrates for terrestrial ecosystems. GSA Today 20, 4–9.

Gu, X., Rempe, D.M., Dietrich, W.E., West, A.J., Lin, T.C., Jin, L., Brantley, S.L., 2020. Chemical reactions, porosity, and microfracturing in shale during weathering: the effect of erosion rate. Geochim. Cosmochim. Acta 269, 63–100.

Helgeson, H.C., Murphy, W.M., Aagard, P., 1984. Thermodynamic and kinetic constraints on reaction rates among minerals and aqueous solutions II. Rate constants, effective surface area, and the hydrolysis of feldspar. Geochim. Cosmochim. Acta 48, 2405–2432.

Hellmuth, K.-H., Siitari-Kauppi, M., 1990. Investigation of the porosity of rocks. Impregnation with ^{14}C-polymethylmethacrylate(PMMA), a new technique. Finland: Finnish Centre for Radiation and Nuclear Safety (STUK).

Hellmuth, K.-H., Siitari-Kauppi, M., Lindberg, A., 1991. Applications of the carbon-14-polymethylmethacrylate (PMMA) impregnation method in studies on porosity and matrix diffusion. MRS Online Proceedings Library Archive 257, 649–656. https://doi.org/10.1557/PROC-257-649.

Hellmuth, K.-H., Siitari-Kauppi, M., Lindberg, A., 1993. Study of porosity and migration pathways in crystalline rock by impregnation with ^{14}C-polymethylmethacrylate. J. Contam. Hydrol. 13, 403–418.

Hellmuth, K.-H., Lukkarinen, S., Siitari-Kauppi, M., 1994. Rock matrix studies with carbon-14-polymethylmethacrylate (PMMA); method development and applications. Isotopenpraxis Isotopes in Environmental and Health Studies 30, 47–60.

Hochella, M.F., Banfield, J.F., 1995. Chemical weathering of silicates in nature: a microscopic perspective with theoretical considerations. Pp. 353-406 in: Chemical Weathering Rates of Silicate Minerals (A.F. White & S.L. Brantley, editors). Reviews in Mineralogy, 31, Mineralogical Society of America.

Jamtveit, B., Putnis, C.V., Malthe-Sørenssen, A., 2009. Reaction induced fracturing during replacement processes. Contrib. Miner. Petrol. 157, 127–133. https://doi.org/10.1007/s00410-008-0324-y.

Jamtveit, B., Kobchenko, M., Austrheim, H., Malthe-Sørenssen, A., Røyne, A., Svensen, H., 2011. Porosity evolution and crystallization driven fragmentation

during weathering of andesite. J. Geophys. Res. Solid Earth 116, B12204. https://doi.org/10.1029/2011JB008649.
Kelokaski, M., Siitari-Kauppi, M., Sardini, P., Möri, A., Hellmuth, K.-H., 2006. Characterisation of pore space geometry by ^{14}C-PMMA impregnation—development work for in situ studies. J. Geochem. Explor. 90, 45–52. https://doi.org/10.1016/jgexplo.2005.09.005.
Ketcham, R.A., Carlson, W.D., 2001. Acquisition, optimization and interpretation of X-ray computed tomographic imagery: applications to the geosciences. Comput. Geosci. 27, 381–400. https://doi.org/10.1016/S0098-3004(00)00116-3.
Kuva, J., Hellmuth, K.-H., Sardini, P., Siitari-Kauppi, M., 2015. Verification of a simulation approach for estimating crack aperture using ^{14}C-PMMA method. J. Coupled Systems Multiscale Dynamics 3, 333–340. https://doi.org/10.1166/jcsmd.2015.1087.
Lebedeva, M.I., Fletcher, R.C., Brantley, S.L., 2010. A mathematical model for steady-state regolith production at constant erosion rate. Earth Surf. Processes Landforms 35, 508–524.
Lee, M.R., Hodson, M.E., Parsons, I., 1998. The role of intragranular microtextures and microstructures in chemical and mechanical weathering: direct comparisons of experimentally and naturally weathered alkali feldspars. Geochim. Cosmochim. Acta 62, 2771–2788.
Lee, M.R., Parsons, I., 1995. Microtextural controls of weathering of perthitic alkali feldspars. Geochim. Cosmochim. Acta 59 (21), 4465–4488.
Leskinen, A., Penttinen, L., Siitari-Kauppi, M., Alanso, U., Garcia-Gutierrez, M., Missana, T., Patelli, A., 2007. Determination of granites' mineral specific porosities by PMMA method and FESEM/EDAX. Scientific Basis for Nuclear Waste Management XXX, 985, 599–604. doi: 10.1557/PROC-985-0985-NN11-20.
Luxmoore, R.J., 1981. Micro-, meso-, and macroporosity of soil. Soil Sci. Soc. Am. J. 45, 671–672.
Maher, K., Chamberlain, C.P., 2014. Hydrologic regulation of chemical weathering and the geologic carbon cycle. Science 343, 1502–1504.
Mazurier, A., Sardini, P., Graham, R.C., Hellmuth, K.H., Parneix, J.C., Rossi, A.M., Siitari-Kauppi, M., Voutilainen, M., Caner, L., 2016. Development of fracture network in crystalline rocks during weathering: study of bishop creek chronosequence using X-ray computed tomography and ^{14}C-PMMA impregnation method. The Geological Society of America Bulletin 128, 1423–1438.
Merino, E., Nahon, D., Wang, Y., 1993. Kinetics and mass transfer of pseudomorphic replacement: application to replacement of parent minerals and kaolinite by Al, Fe, and Mn oxides during weathering. Am. J. Science 293, 135–155.
Meunier, A., Sardini, P., Robinet, J.C., Prêt, D., 2007. The petrography of weathering processes: facts and outlooks. Clay Miner. 42, 415–435.
Moon, S., Perron, J.T., Martel, S.J., Holbrook, W.S., St. Clair, J., 2017. A model of three-dimensional topographic stresses with implications for bedrock fractures, surface processes, and landscape evolution. J. Geophys. Res. Earth Surf. 122, 823–846. https://doi.org/10.1002/2016JF004155.
Navarre-Sitchler, A., Brantley, S.L., 2007. Basalt weathering across scales. Earth Planet. Sci. Lett. 261, 321–334.
Navarre-Sitchler, A., Steefel, C.I., Yang, L., Tomutsa, L., 2009. Evolution of porosity and diffusivity associated with chemical weathering of a basalt clast. J. Geophys. Res. Earth Surf. 114, F02016.
Navarre-Sitchler, A., Cole, D.R., Rother, G., Jin, L., Buss, H.L., Brantley, S.L., 2013. Porosity and surface area evolution during weathering of two igneous rocks. Geochim. Cosmochim. Acta 109, 400–413.
Navarre-Sitchler, A., Brantley, S.L., Rother, G., 2015. How porosity increases during incipient weathering of crystalline silicate rocks. Rev. Mineral. Geochem. 80, 331–354. https://doi.org/10.2138/rmg.2015.80.10.
Oila, E., Sardini, P., Siitari-Kauppi, M., Hellmuth, K.-H., 2005. The ^{14}C-polymethylmethacrylate (PMMA) impregnation method and image analysis as a tool for porosity characterization of rock-forming minerals. Geological Society, London, Special Publications 240, 335–342. https://doi.org/10.1144/GSL.SP.2005.240.01.24.
Puche, N., Le Mer, G., Jouquet, P., Mazurier, A., Caner, L., Garnier, P., Tran, M.T., Rumpel, C., 2022. Mechanisms and kinetics of physical protection of soil organic carbon in earthworm casts in tropical environment. Soil Biol. Biochem. 170 https://doi.org/10.1016/j.soilbio.2022.108686.
Putnis, A., 2002. Mineral replacement reactions: from macroscopic observations to microscopic mechanisms. Mineral. Mag. 66, 689–708. https://doi.org/10.1180/0026461026650056.
Putnis, A., 2009. Mineral replacement reactions. Rev. Mineral. Geochem. 70, 87–124. https://doi.org/10.2138/rmg.2009.70.3.
Putnis, A., 2015. Transient porosity resulting from fluid-mineral interaction and its consequences. Rev. Mineral. Geochem. 80, 1–23. https://doi.org/10.2138/rmg.2015.80.01.
Robin, V., Sardini, P., Mazurier, A., Regnault, O., Descostes, M., 2016. Effective porosity measurements of poorly consolidated materials using non-destructive methods. Eng. Geol. 205, 24–29.
Robinet, J.C., Sardini, P., Coelho, D., Parneix, J.C., Prêt, D., Sammartino, S., Boller, E., Altmann, S., 2012. Effects of mineral distribution at mesoscopic scale on solute diffusion in a clay-rich rock: Example of the Callovo-Oxfordian mudstone (Bure, France): Water Resources Research, v. 48, W05554. doi: 10.1029/2011WR011352.
Robinet, J.C., Sardini, P., Siitari-Kauppi, M., Prêt, D., Yven, B., 2015. Upscaling the porosity of the Callovo-Oxfordian mudstone from the pore scale to the formation scale;insights from the ^{3}H-PMMA autoradiography technique and SEM BSE imaging. Sed. Geol. 321, 1–10.
Rossi, A.M., Graham, R.C., 2010. Weathering and porosity formation in subsoil granitic clasts, Bishop Creek moraines, California. Soil Sci. Soc. Am. J. 74, 172–185.
Sammartino, S., Siitari-Kauppi, M., Meunier, A., Sardini, P., Bouchet, A., Tevissen, E., 2002. An imaging method for the porosity: adjustment of the PMMA method – example of a calcareous shale characterization. J. Sediment. Res. 72 (6), 937–943.
Sardini, P., Siitari-Kauppi, M., Beaufort, D., Hellmuth, K.-H., 2006. On the connected porosity of mineral aggregates in crystalline rocks. Am. Mineral. 91, 1069–1080.
Sardini, P., El Albani, A., Prêt, D., Gaboreau, S., Siitari-Kauppi, M., Beaufort, D., 2009. Mapping and quantifying the clay aggregates microporosity in medium to coarse grained sandstones using the ^{14}C-PMMA method. J. Sediment. Res. 79, 584–592.
Sardini, P., Caner, L., Mossler, P., Mazurier, A., Hellmuth, K.-H., Graham, R.C., Rossi, A. M., Sardini, P., Kuva, J., Siitari-Kauppi, M., Hellmuth, K.-H., 2014. A simplified simulation approach for estimating crack aperture using ^{14}C-PMMA method. J. Coupled Systems Multiscale Dyn. 2, 244–255. https://doi.org/10.1166/jcsmd.2014.1053.
Schlüter, S., Roussety, T., Rohe, L., Guliyev, V., Blagodatskaya, E., Reitz, T., 2021. Land use impact on carbon mineralization is mainly caused by variation of particulate organic matter content rather than of soil structure. Soil. https://doi.org/10.5194/soil-2021-56.
Siitari-Kauppi, M., 2002. Development of ^{14}C-polymethylmethacrylate method for the characterisation of low porosity media: Application to rocks in geological barriers of nuclear waste storage (Doctoral dissertation). Helsinki, Finland. Retrieved from https://helda.helsinki. fi/bitstream/handle/10138/21122/developm.pdf.
Soille, P., 2004. Morphological Image Analysis: Principles and Applications: Berlin, Springer-Verlag, 391 p.
St. Clair, J., Moon, S., Holbrook, W. S., Perron, J. T., Riebe, C. S., Martel, S. J., Carr, B., Harman ,C., Singha, K., deB. Richter, D. (2015): Geophysical imaging reveals topographic stress control of bedrock weathering. Science 350 (6260): 534-538. doi: 10.1126/science.aab2210.
Velde, B., Meunier, A., 2008. The Origin of Clay Minerals in Soils and Weathered Rocks. Springer, 407 pp.
Voutilainen, M., Siitari-Kauppi, M., Sardini, P., Lindberg, A., Timonen, J., 2012. Pore-space characterization of an altered tonalite by Xray computed microtomography and the ^{14}C-labeled-polymethylmethacrylate method. J. Geophys. Res. Solid Earth 117 (B1), 14. https://doi.org/10.1029/2011JB008622.
White, A.F., Brantley, S.L., 2003. The effect of time on the weathering of silicate minerals: why do weathering rates differ in the laboratory and field? Chem. Geol. 202, 479–506.
White, A.F., Blum, A.E., Schulz, M.S., Huntington, T.G., Peters, N.E., Stonestrom, D.A., 2002. Chemical weathering of the Panola Granite: Solute and regoliths elemental fluxes and the weathering rate of biotite. Water Rock Interactions, Ore Deposits, and Environmental Geochemistry: A Tribute to David A. Crerar, 37–59.
White, A. F., Peterson, M.L., 1990. Role of reactive-surface-area character-ization in geochemical kinetic-models, in Melchior D.C., Bassett, R.L. (Eds.), Chemical Modeling of Aqueous Systems, II, ACS Symp. Am. Chem. Soc., Washington, D. C., pp. 461–475.